Contrib Mineral Petrol (2002) 142: 738–752
DOI 10.1007/s00410-001-0325-6

A. Mulch · M.A. Cosca · M.R. Handy

In-situ UV-laser $^{40}Ar/^{39}Ar$ geochronology of a micaceous mylonite : an example of defect-enhanced argon loss

Received: 21 June 2001 / Accepted: 15 October 2001 / Published online: 13 December 2001

Abstract Muscovite and biotite from a crustal-scale mylonite zone (Pogallo Shear Zone, southern Alps) were investigated using furnace step-heating and in-situ UV-laser ablation $^{40}Ar/^{39}Ar$ geochronology. Undeformed muscovite porphyroclasts yield $^{40}Ar/^{39}Ar$ plateau ages of 182.0 ± 1.6 Ma, whereas in-situ UV-laser ablation $^{40}Ar/^{39}Ar$ dating and furnace step-heating of strongly deformed muscovite and biotite grains display a range of apparent ages that are systematically younger. The range of $^{40}Ar/^{39}Ar$ ages measured in the deformed muscovite and biotite is consistent with protracted cooling through argon closure in minerals that exhibit variably developed segmentation on the intra-grain scale. These microstructurally controlled segments are bound by either first-order lattice discontinuities, sub-microscopic structural defects and/or zones of high defect density, which create variable length-scales for intragranular argon diffusion. The observed deformational microstructures within muscovite and biotite acted as intra-grain fast diffusion pathways in the slowly cooled mylonitic rocks. Therefore, the high-spatial resolution $^{40}Ar/^{39}Ar$ data record the initial and final closure to argon diffusion over a time span of about 60 Ma.

Introduction

The $^{40}Ar/^{39}Ar$ method has great potential for resolving discrete phases of deformation in orogenic systems if the temperature–time–deformation relationships between fabric-forming minerals amenable to isotopic dating and the tectonic history are evaluated critically. A combination of microstructural analyses, chemical microanalyses and X-ray diffraction data with $^{40}Ar/^{39}Ar$ geochronological data can provide important information on the deformational and crystallization history of minerals (e.g. Dunlap et al. 1991; West and Lux 1993; Kontak et al. 1996; Dunlap 1997; Reddy et al. 1997, 1999, 2001; Jaboyedoff and Cosca 1999). Crustal mylonite zones are excellent structures for studying such relationships because strain is localized and field observations are often sufficiently precise to define the relative timing of fabric development. In such areas it is critical to fully understand the relationship between the time of mineral crystallization and/or recrystallization and any $^{40}Ar/^{39}Ar$ data obtained from them. Despite the wide application of the $^{40}Ar/^{39}Ar$ technique, however, mechanisms controlling argon retention in these minerals are not well understood. Therefore, the processes that govern argon retention (or loss) from such minerals need to be sufficiently characterized if the data are to be used for reconstructing accurate tectonic and/or thermochronological histories.

Studies applying $^{40}Ar/^{39}Ar$ laser microprobe techniques have shown that single mineral grains from diverse geological environments often preserve significant radiogenic argon ($^{40}Ar^*$) concentration gradients (e.g. Phillips and Onstott 1988; Lee et al. 1990; Scaillet et al. 1990; Kelley and Turner 1991; Hames and Bowring 1994; Hodges and Bowring 1995; Reddy et al. 1996; Hames and Andresen 1996; Hames and Cheney 1997; Giorgis et al. 2000; Kramar et al. 2001). Different mechanisms have been invoked to explain the various argon concentration gradients including the introduction of excess argon (Reddy et al. 1996; Sherlock et al. 1999), re-equilibration with a changing external argon reservoir during retrograde metamorphism (Giorgis et al. 2000) and argon concentration profiles that reflect diffusive-loss gradients (e.g. Hodges and Bowring 1995; Hames and Andresen 1996; Kramar et al. 2001). For the

A. Mulch (✉) · M.A. Cosca
Institut de Minéralogie et Géochimie,
Université de Lausanne, BFSH-2,
1015 Lausanne, Switzerland
E-mail: andreas.mulch@img.unil.ch

M.R. Handy
Institut für Geowissenschaften,
Freie Universität Berlin, Malteserstrasse 74-100,
12249 Berlin, Germany

Editorial responsibility: J Hoefs

case of micas in mylonitic rocks, the application of high-spatial resolution ultraviolet (UV) lasers in $^{40}Ar/^{39}Ar$ studies (e.g. Kelley et al. 1994) and refined mass spectrometer sensitivity provide the means to determine directly the relationship between microstructures and $^{40}Ar^*$ concentrations within individual thin sections and individual minerals. However, the effects of microstructure development and their importance on argon isotope behaviour are considered in very few studies (e.g. Lee 1995; Hames and Cheney 1997; Reddy et al. 1999, 2001; Kramar et al. 2001). A better understanding of the interaction between deformation, microstructure development and argon isotope systematics requires an integrated approach using high spatial resolution dating techniques together with detailed characterization of the sample. Although transmission electron microscopy (TEM) permits direct measurement of dislocation densities and distributions within a mineral lattice, the scale of TEM observations differs by orders of magnitude from the minimum laser spot size required for UV-laser ablation $^{40}Ar/^{39}Ar$ geochronology. Characterizing the spatial distribution of major lattice discontinuities by back-scattered electron (BSE) imaging and optical microscopy is a means of identifying intra-grain microstructures on the same scale as the spatial resolution of the $^{40}Ar/^{39}Ar$ UV-laser microprobe and thus permits the direct comparison of both data sets. Another promising approach is the use of orientation contrast imaging through fore-scatter electron microscopy as shown in a recent study by Reddy et al. (2001).

In order to assess the effects of deformation on $^{40}Ar/^{39}Ar$ geochronological results, especially in terms of argon loss and closure temperature (Dodson 1973), we present high-spatial resolution in-situ UV-laser ablation $^{40}Ar/^{39}Ar$ data from variably deformed muscovite and biotite grains within a crustal-scale mylonite of the Ivrea Verbano Zone (IVZ), Italy. The abundant field and available isotopic data demonstrate unequivocally that the IVZ underwent protracted cooling following mylonitization, making this unit a perfect field laboratory for the investigation of diffusive argon loss in naturally deformed minerals. When combined with field and microstructural observations, the $^{40}Ar/^{39}Ar$ results are used to demonstrate that deformation is a key factor controlling argon loss in micas, primarily by acting to decrease the effective length-scale for argon diffusion. These results show that for the investigated rocks, the range of observed muscovite and biotite ages are consistent with regional geological constraints on slow cooling of the IVZ.

Geological setting

The S–C mylonite in this study comes from the central part of the Pogallo Shear Zone (PSZ; Hodges and Fountain 1984; Fig. 1), a crustal-scale shear zone with a well-known structural and metamorphic history (e.g. Handy 1987; Handy and Zingg 1991). The PSZ is a ca. 3-km-wide steeply dipping zone of oblique sinistral mylonitic shear that accommodated exhumation of the Ivrea-Verbano Zone (IVZ) with respect to the Strona-Ceneri Zone (SCZ,

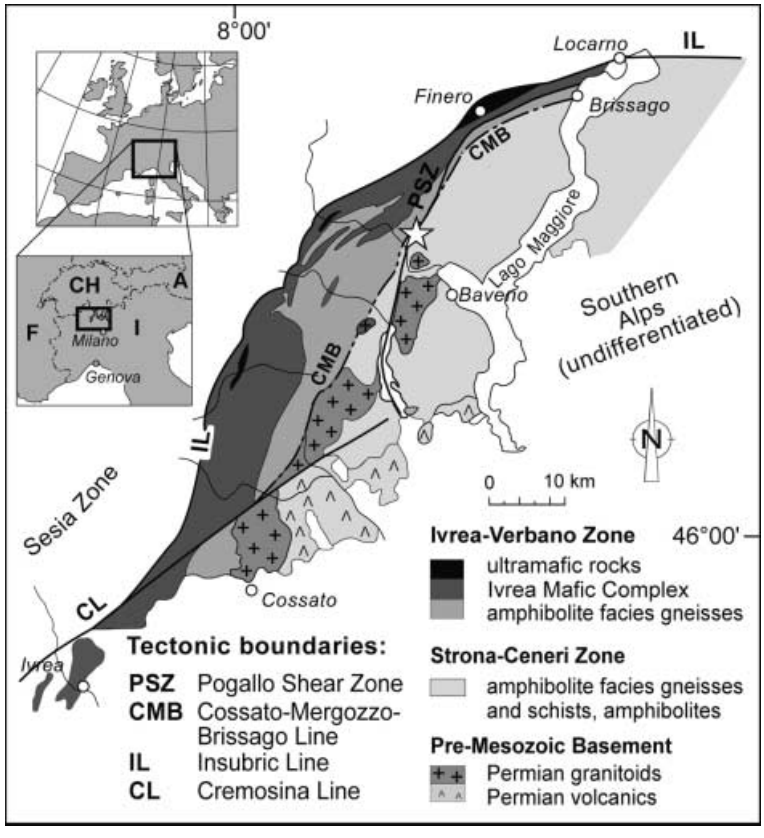

Fig. 1 Tectonic map of the basement and cover units in the western part of the southern Alps. The *white star* marks the sample location within the central part of the Pogallo Shear Zone

Fig. 1). Mylonitization primarily affected the IVZ under retrograde amphibolite to greenschist facies conditions (Handy 1987). The presently steep dip of the mylonitic foliation results from Tertiary Insubric folding and thrusting (Schmid et al. 1987). When back-rotated into its original pre-Alpine orientation, the PSZ acquires a moderate to shallow dip and accommodated E–W-directed lateral crustal extension (Handy 1987). Cross-cutting relationships in the field place broad time constraints on the age of Pogallo mylonitization. The Pogallo mylonites overprint Early Permian mafic dikes (Boriani and Sacchi 1973; Mulch et al. 2002) and granitoids, but are themselves truncated by brittle faults related to Tertiary Insubric tectonics (Handy 1987). Correlating the temperatures of syntectonic, retrograde metamorphism within the Pogallo mylonites (300–500 °C) with the geochronologically derived cooling curve for the southern IVZ, yields an age of 170–220 Ma for mylonitization along the PSZ (Zingg et al. 1990; Handy and Zingg 1991). This broad age range coincides with that of syn-rift sediments in half-grabens preserved in the cover of the southern Alpine basement (Winterer and Bosellini 1981). Like the PSZ, these half-grabens accommodated E–W-directed lateral extension and were kinematically linked to mylonitization along the PSZ. Rifting and development of sedimentary unconformities in these half-grabens began in the Norian (~220 Ma) and ended during the Late Liassic (~180 Ma; Bertotti et al. 1993, 1999). Therefore, the PSZ is interpreted as an intermediate to deep crustal shear zone that accommodated rifting of the Apulian continental margin just prior to the Late Jurassic opening of the Ligurian Ocean (Handy and Zingg 1991). Basin subsidence and spreading that post-date the Early Jurassic rifting of the Liguro–Piemontese basin were associated with the formation of oceanic crust and deposition of undisturbed pelagic sediments (Winterer and Bosellini 1981). This evolution is also documented by geochronological studies of Alpine ophiolites, which demonstrate that crustal extension within the basin was associated with gabbroic intrusions at around 164–166 Ma (e.g. Bill et al. 1997; Rubatto et al. 1998).

Metamorphic titanite within Early Permian mafic intrusive rocks near the PSZ yields a concordant U–Pb growth age of 173 ± 4 Ma, which is interpreted to date the breakdown of hornblende and ilmenite during retrograde metamorphism and uplift of the IVZ (Mulch et al. 2002). This U–Pb age is consistent with the range of mica cooling ages observed in the IVZ (e.g. Hunziker et al. 1992). These Mid-Jurassic ages are related to exhumation and cooling associated with mylonitization and lateral crustal extension along the PSZ. The 173 ± 4 Ma titanite growth age represents the best available estimate for the timing of retrograde metamorphism in the IVZ caused by differential uplift along the PSZ. As expected for slow thermal equilibration of two tectonically juxtaposed geological units, metamorphic mineral reactions in the IVZ footwall occur with a certain time lag with respect to the onset of deformation. Therefore, the retrograde titanite growth at 173 ± 4 Ma post-dates the actual age of Pogallo mylonitization (see below).

Sample description and microstructures within Pogallo mylonites

Strongly deformed muscovite–biotite schists from the central part of the PSZ contain a mineral assemblage of dynamically recrystallized quartz, K-feldspar, biotite, muscovite, fibrolitic sillimanite and accessory zircon. There is clear evidence from thin section observations for three microstructurally distinct populations of muscovite in the Pogallo mylonites. These populations include porphyroclastic micas defining the main mylonitic schistosity (S), which show evidence of marginal dissolution and mechanical segregation associated with the mylonitic deformation event. In addition, there are micas within extensional shear bands (C′-surfaces of Vauchez 1987) that represent neocrystallized grains that formed during progressive stages of deformation. In thin section, coherent lattice domains in muscovite from the Pogallo mylonites are bound by first-order discontinuities, such as high- and low-angle kink bands, zones of high defect density and/or undulatory extinction, isolated lens-shaped kink bands and discrete intragranular microfractures. Wilson and Bell (1979) introduced the term 'segmentation' for such white mica to describe a process that includes distortion of the white mica lattice accompanied by intracrystalline fracturing.

Type I muscovites are porphyroclasts (Fig. 2a) that form within the main mylonitic (S) foliation and consist of millimetre-sized grains that are often associated with early syn-kinematic fibrolitic sillimanite. Grain boundary diffusion associated with marginal dissolution that apparently occurred during early stages of deformation results in an irregular external shape of most of the type I porphyroclasts (Fig. 2a). Type I muscovite grains are generally characterized by abundant lattice misorientations and internal displacement across the (001) cleavage planes to result in a regularly oriented (but heterogeneously-spaced and -sized) grain segmentation. Internal displacement is commonly accommodated by high-angle kink bands that significantly offset the (001) planes and taper towards a point where they terminate as rectilinear low-angle kink bands. These are defined by 2–5-μm-wide cleavage partings that gently bend the (001) cleavage by about 3–8° (Fig 2d, e). High-angle kink bands are usually triangular in shape and bounded laterally by intragranular microfractures that propagate from internal parts of the grain towards the grain boundaries (inset in Fig. 2d). However, spatially isolated lens-shaped kink bands with lengths of up to 100 μm and coplanar micro-kinks at approximately

►

Fig. 2a–e Photomicrographs of Pogallo microstructures. **a** Type I muscovite porphyroclast (*ms I*) within mylonitic foliation (*S*) adjacent to a C′-shear band. Deformation of the porphyroclast results in segmentation of the grain, introduction of intragranular fractures and zones of undulatory extinction. Note the heterogeneous spacing of segment-bounding dislocation bands at right angles to the {001} cleavage. **b** Segmented type II muscovite grains (*ms II*) situated within a mylonitic C′-shear band of recrystallized biotite (bt_{rx}). Type II grains are inferred to have formed by mechanical segregation and slip along the basal cleavage plane of type I porphyroclasts. **c** Anastomosing mylonitic C′-shear bands defined by fine-grained recrystallized biotite. Note the preservation of dynamic microstructures in recrystallized quartz and the presence of syn-mylonitic type III muscovite grains (*ms III*). Geometrical relationship between S- and C′-surfaces is identical for **a–c** and indicated in **c**. **d** Close-up of segmented type I muscovite porphyroclast in **a** with regularly oriented microfractures and segment-bounding kink bands that separate microstructurally controlled segments (*mcs*). Individual, triangular-shaped kink bands are occasionally bounded by intragranular fractures and taper to a point where strain is accommodated by the formation of gentle, low-angle kink bands that offset (001) by only a few degrees. **e** Type I muscovite deformed by a combination of kinking during cleavage-parallel shortening and fracturing across cleavage planes. All photos taken under crossed polarizers. *Scale* is given at the lower left of each figure. *qtz* quartz; *bt* biotite

right angles to the (001) plane have been observed in the proximity of C′-shear bands where the internal strain within type I muscovites is greatest. Both show remarkably constant cleavage displacements, consistent with the overall sense-of-shear in the mylonite (Simpson and Schmid 1983; Lister and Snoke 1984) and form major lattice discontinuities across the (001) cleavage planes. The variety of microstructures described above require a combination of deformation mechanisms involving basal dislocation glide within the K-interlayer (e.g. Banos et al. 1983), formation of kink band boundaries and microfractures caused by shortening within the basal cleavage plane (e.g. Bell et al. 1986; Goodwin and Wenk 1990; Shea and Kronenberg 1992; Mares and Kronenberg 1993) and dilation along the basal cleavage plane ('cleavage partings'; e.g. Goodwin and Wenk 1990).

Type II muscovite grains are formed by cleavage-parallel segregation of type I porphyroclasts during progressive deformation (Fig. 2b). The type II grains display extremely variable grain sizes ranging from a few tens to several hundred micrometres. They are commonly rotated into C′-shear bands where they occur as 'foliation fish' according to the nomenclature of Passchier and Trouw (1996). Mica 'foliation fish' of type II described here are common in mylonitic rocks where pre-existing large muscovite grains are deformed by a combination of brittle and crystal–plastic processes (Lister and Snoke 1984). Deformation of type II muscovites is predominantly by dislocation glide within the

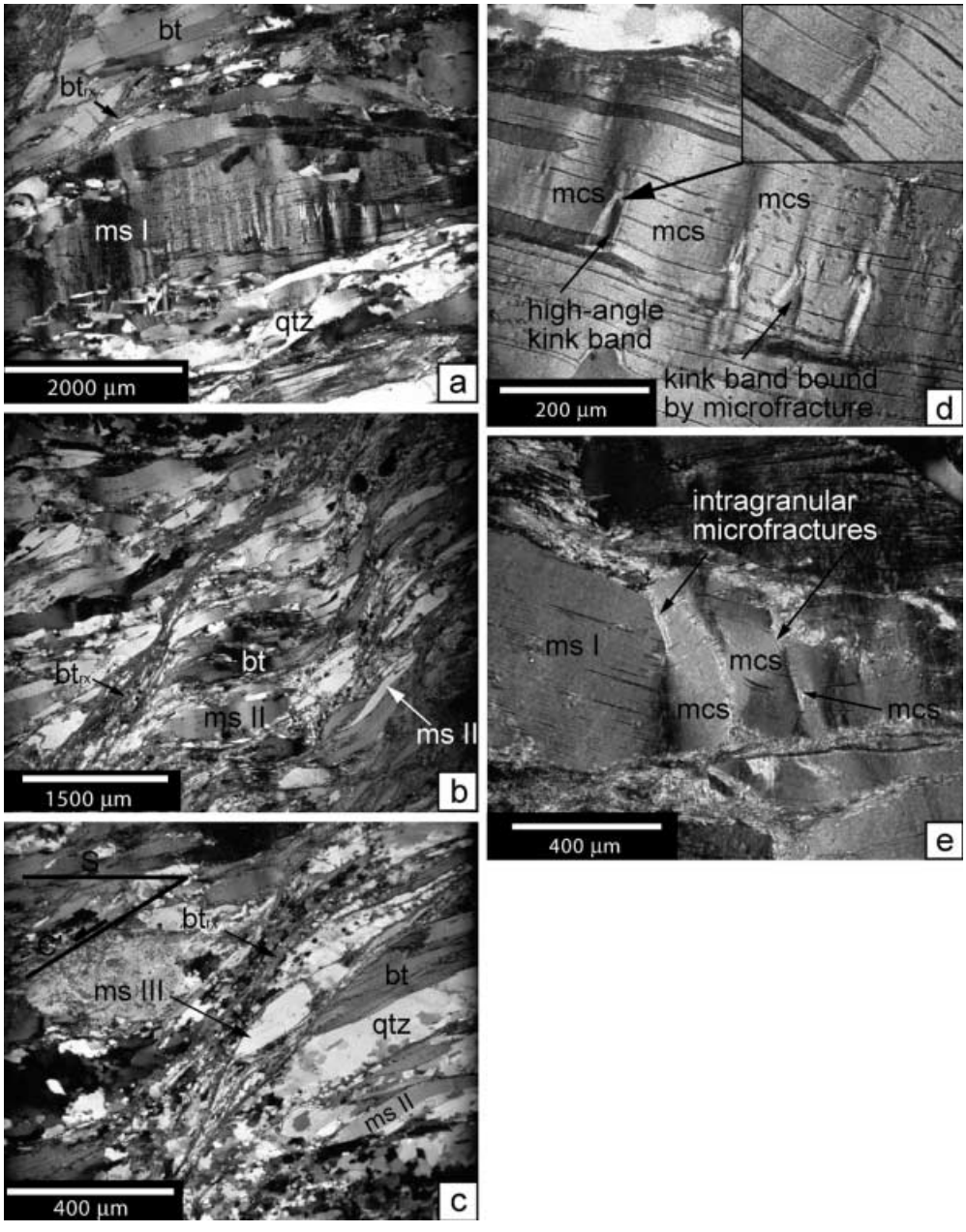

basal cleavage plane and is associated with the development of kink bands.

Acicular muscovite grains of type III are smaller, usually in the range of 100–200 μm (Fig. 2c). These grains display evidence of intracrystalline glide and/or occasionally boudinage. They occur within very fine grained, syn-kinematic biotite–chlorite trails that crystallized during the activity of the C′-shear bands. The intimate spatial association with synkinematic biotite within C′-shear bands, and a subtle difference in muscovite composition (see Table 1) are taken as evidence that the type III muscovite grains are neocrystallized micas that formed during Pogallo mylonitization.

Microstructures for muscovite types I–III suggest that both diffusion- and strain-controlled deformation mechanisms were active during mylonitization, which probably reflects progressively lower deformation temperatures during the retrograde evolution of the shear zone. Type I muscovites are thought to represent pre-kinematic porphyroclasts, probably formed during late/post Variscan metamorphism in the IVZ metasediments (e.g. Handy et al. 1999). In contrast, type II muscovites are interpreted to have formed by mechanical segregation of type I porphyroclasts during Pogallo mylonitization because of continuous basal slip along the (001) cleavage planes whereas type III muscovites formed by neocrystallization within the C′-shear bands. All three types of muscovite described here occur within a mylonitic matrix of dynamically recrystallized quartz. The microstructural fabric in the quartz-rich domains is characterized by flattened quartz grains oriented parallel to the S-foliation. The oblique, shape-preferred orientation in these dynamically recrystallized quartz aggregates is consistent with a sinistral sense-of-shear and with that deduced from dilatant C′-shear bands. Matrix quartz shows abundant subgrain formation and recrystallization by subgrain rotation and grain boundary migration (Fig. 2c). K-feldspar rotates passively in the quartz matrix and shows internal fracturing. This limits the syn-tectonic temperatures to below those necessary for dislocation glide and creep in feldspar (500–550 °C at natural strain rates; Tullis 1983). Preservation of strong grain size gradients in zones of stress concentration (as, e.g. around competent K-feldspar porphyroclasts or along shear bands) indicates that dynamic quartz microstructures never experienced sufficiently high temperatures (300–320 °C, Masuda et al. 1997) to induce static annealing after mylonitic deformation had ceased. Muscovite and quartz from the same split used for $^{40}Ar/^{39}Ar$ furnace step-heating were also analysed for their oxygen isotope composition. Oxygen isotope thermometry yielded an equilibrium temperature of 430 ± 40 °C, which is in good agreement with the observed stable mylonitic paragenesis and temperature estimates from microstructural observations.

Analytical procedure

The deformation history of the central part of the PSZ was characterized by carefully examining the structural relationships recorded in the mylonitic Ivrea metasediments and in the adjacent Strona-Ceneri Zone. Based on a detailed outcrop map containing pertinent structural and lithological data, microstructure development in the sampled mylonite could be unequivocally assigned to larger scale observations. A disk 18 mm in diameter and 300 μm thick was drilled from a polished thick section oriented parallel to the XZ-fabric plane (i.e. the plane parallel to the mylonitic lineation, but perpendicular to the foliation) of micaceous mylonite from the IVZ footwall of the PSZ. An oriented thin section was prepared from the opposite face of the disk and was examined by optical microscopy and back-scattered electron imaging. The disk, bulk minerals and closely spaced standards were irradiated in the central thimble position of the USGS TRIGA reactor in Denver (CO), USA (Dalrymple et al. 1981). The neutron flux was monitored using the standard MMHB-1 assuming an age of 523.1 ± 4.6 Ma (Renne et al. 1998). Furnace step-heating analyses were made

Table 1 Microprobe analyses of muscovite from the Pogallo mylonites. *n.d.* Not determined (below detection limit)

	Type I[a]	SD[b] ($n=60$)	Type II[a]	SD[b] ($n=30$)	Type III[a]	SD[b] ($n=30$)
SiO_2	45.64	(0.33)	45.90	(0.42)	45.70	(0.31)
TiO_2	0.74	(0.15)	0.70	(0.10)	0.49	(0.07)
Al_2O_3	35.57	(0.15)	35.69	(0.53)	35.82	(0.26)
Cr_2O_3	0.00	(0.00)	0.01	(0.02)	0.01	(0.02)
FeO^t	1.25	(0.11)	1.29	(0.28)	1.31	(0.21)
MnO	n.d.	–	n.d.	–	n.d.	–
MgO	0.55	(0.04)	0.55	(0.11)	0.56	(0.07)
BaO	0.06	(0.14)	0.07	(0.18)	0.42	(0.14)
CaO	n.d.	–	n.d.	–	n.d.	–
Na_2O	0.48	(0.04)	0.42	(0.05)	0.44	(0.03)
K_2O	10.68	(0.10)	10.77	(0.14)	10.68	(0.14)
Cl	n.d.	–	n.d.	–	n.d.	–
Total	94.97	(0.34)	95.40	(0.65)	95.43	(0.29)
$Si_{IV}/(Si_{IV}+Al_{IV})$	0.763		0.764		0.763	
$(Fe+Mg)/Al_{VI}$	0.067		0.068		0.069	
$Na/(Na+K)$	0.064		0.056		0.059	

[a]Average value of n analyses across single muscovite grains
[b]Standard deviation of n analyses

using a double vacuum resistance furnace. The laser analyses were done using a pulsed excimer (KrF) laser operating at a wavelength of 248 nm. In general, the size and depth of the ablation pits were varied to obtain ^{40}Ar signals at least ten times the blank values. For this study, a spot size of about 50×50 μm was used and ablation pits were excavated to an estimated depth of about 30 μm during a 60-s ablation interval. The UV-laser ablation produced well-defined rectangular pits within muscovite and biotite grains (Fig. 3). No thermal alteration or deformation [e.g. splitting parallel to (001) cleavage or cracking of the grains] at the exterior of the ablation pit was observed during the analyses. After ablation (or furnace step-heating), the gas was gettered using activated Zr–Ti–Al getters and exposed to a metal cold finger at temperatures of approximately –130 °C for an additional 180 s to remove all active gases. Following cleanup, the gas was expanded into a Brunner-modified MAP 215-50 mass spectrometer for isotopic analysis. Eight scans per analysis were made over the mass range of 40 to 36. System blanks measured over the time of an analysis were subtracted from the overall signal. A typical in-situ UV-laser blank measurement yielded the following results: $^{40}Ar = 7.8\times10^{-17}$ mol; $^{39}Ar = 3.3\times10^{-18}$ mol; $^{38}Ar = 1.9\times10^{-18}$ mol; $^{37}Ar = 1.4\times10^{-18}$ mol; $^{36}Ar = 3.4\times10^{-18}$ mol. Furnace blanks ranged for mass 40 from 2×10^{-14} mol at 1,500 °C to 5×10^{-15} mol below 1,000 °C. Blank values for masses 36–39 were below 2×10^{-16} mol. Peak heights above background were corrected for mass discrimination, and for decay of interfering nucleogenic isotopes of argon derived from Ca, K and Cl. The apparent ages were calculated using an assumed initial $^{40}Ar/^{36}Ar$ ratio of 295.5 and decay constants recommended by Steiger and Jäger (1977). Age uncertainties are reported throughout at the 2σ confidence level and include the error in J. Oxygen isotope data were obtained in muscovite and quartz by laser fluorination following the procedures outlined by Sharp (1992), with the modification that elemental O_2 was analysed directly. Oxygen isotope thermometry results are calculated using the fractionation factors of Chacko et al. (1996). Back-scattered electron (BSE) imaging was performed on a CamScan SEM using 20 kV accelerating potential.

In-situ $^{40}Ar/^{39}Ar$ UV-laser ablation

Three type III muscovite grains, each measuring ~80×160 μm across oriented parallel to C′-shear bands, were analysed by in-situ $^{40}Ar/^{39}Ar$ UV-laser ablation. In addition, several spot traverses were made across type I muscovite porphyroclasts that define the main mylonitic (S) foliation. In-situ $^{40}Ar/^{39}Ar$ dates of analysed muscovite grains are highly variable when measured perpendicular to the [001] direction (i.e. with the laser beam parallel to the {001} cleavage) of individual, deformed grains (Fig. 4). This orientation is different from the orientation generally used in diffusion studies with the [001] direction being parallel to the laser beam (e.g. Hodges and Bowring 1995; Hames and Andresen 1996). However, as platy minerals such as micas rotate into the shear plane of a foliated rock during progressive deformation their structural relationship can only be analysed within the XZ fabric plane. Analysing sections of muscovite with the laser beam parallel to the (001) plane is more difficult for determining argon diffusion profiles, but is the only way to directly compare intra-grain age variations and deformational microstructures.

The $^{40}Ar/^{39}Ar$ ages for type I muscovites span a range of about 65 Ma and individual muscovite grains reveal

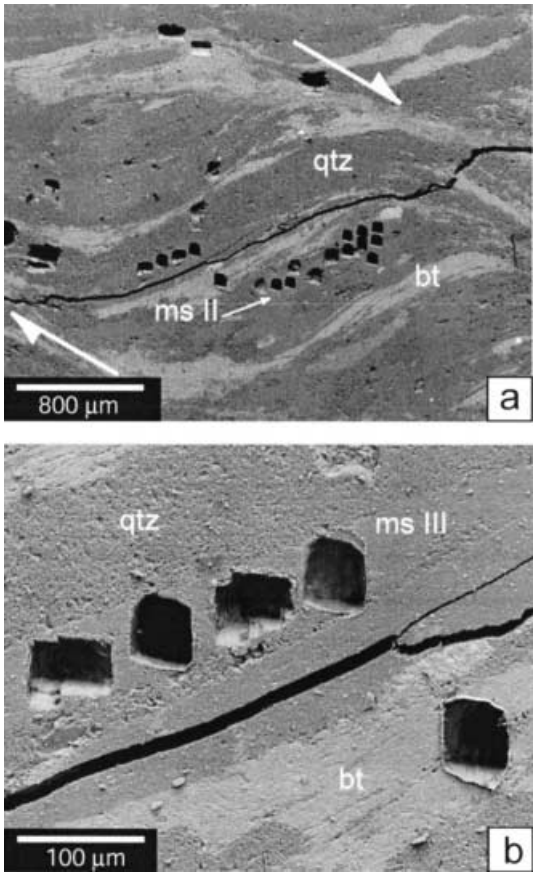

Fig. 3 **a** Back-scattered electron (BSE) image of in-situ UV-laser ablation pits within type II muscovite (*ms II*) situated within a C′-shear band (*white arrows*). **b** BSE image documenting the high-spatial resolution of four UV-laser analyses within a type III muscovite grain adjacent to recrystallized matrix quartz (*qtz*). The prominent crack is a result of sample preparation. *bt* Matrix biotite

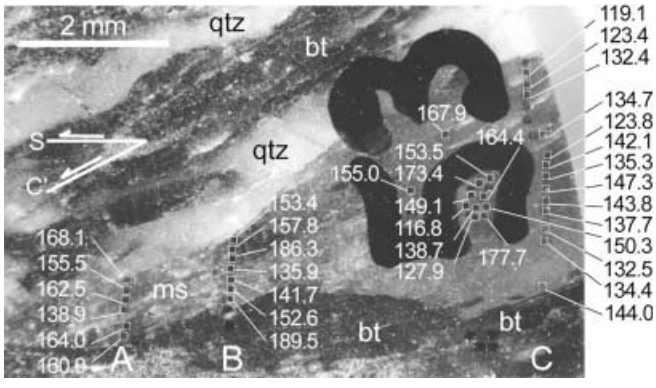

Fig. 4 Photograph of type I muscovite porphyroclast showing location of in-situ UV-laser ablation pits and $^{40}Ar/^{39}Ar$ dates (in Ma). Individual errors on each analysis are of the order of ±5%. Deformation adjacent to a C′-shear band results in a significant reduction in thickness of the porphyroclast to yield highly variable $^{40}Ar/^{39}Ar$ dates. *A*, *B*, and *C* correspond to vertical age traverses referred to in the text

a strongly heterogeneous $^{40}Ar^*$ distribution (Fig. 4). A histogram plot (Fig. 5) shows a near-Gaussian distribution of the apparent $^{40}Ar/^{39}Ar$ ages for both type I

and III muscovites, with error-weighted averages of 147.7 ± 5.1 and 147.3 ± 6.5 Ma, respectively. The oldest apparent ages of type I muscovites are identical within error to ages derived by incremental step-heating of undeformed muscovite porphyroclasts from the same sample (see below). Analyses of mixtures of very fine-grained recrystallized biotite and quartz within mylonitic shear bands (e.g. 15UL-5.3) reveal anomalously old $^{40}Ar/^{39}Ar$ apparent ages, perhaps because of the presence of excess argon within quartz fluid inclusions. In-situ UV-laser $^{40}Ar/^{39}Ar$ biotite data were obtained on several grains dispersed throughout the entire sample and are interpreted to be representative of deformed biotite in the mylonite. The apparent ages also cover a large range of about 55 million years but are shifted to consistently lower values with respect to the results of deformed muscovite. As with the muscovite data, a histogram plot reveals a near-Gaussian distribution of the $^{40}Ar/^{39}Ar$ apparent ages, with an error-weighted average of 123.3 ± 7.2 Ma.

$^{40}Ar/^{39}Ar$ furnace step-heating

Bulk separates (1.5–8 mg) of deformed and undeformed muscovite splits of the investigated sample were analysed by $^{40}Ar/^{39}Ar$ furnace step-heating (Table 2). The experiments performed on undeformed grains were restricted to the 355–500-μm (20UL-28) and 500–2,000-μm (20UL-25) fractions to avoid dating mixtures of type I and III muscovites. Deformed grains of the 355–500-μm fraction (20UL-27) were carefully selected under a binocular microscope and exhibit kink band formation, bending and tight folding of the basal cleavage plane. Muscovites within all samples were free of microscopic impurities, resulting in very pure concentrates after manual selection. The step-heating $^{40}Ar/^{39}Ar$ age spectra of analyses 20UL-28 and 20UL-25 are essentially flat (Fig. 6) and analytically indistinguishable at the 2σ error level. Split 20UL-25 gave a plateau age of 182.7 ± 2.4 Ma for the interval of 5–65% of ^{39}Ar released, and split 20UL-28 forms a plateau of 181.4 ± 2.2 Ma (24–100% ^{39}Ar released) that overlaps within the error. The $^{40}Ar/^{39}Ar$ age spectrum for the deformed muscovite split (20UL-27) forms a double-staircase spectrum with apparent ages rising from 85.7 ± 0.4 to 180.6 ± 0.7 Ma. The highest temperature degassing step overlaps within 2σ error limits with the plateau ages of the two undeformed sample splits.

Isotopic closure temperatures

Many geochronological and tectonic studies apply the concept of isotopic 'closure temperature' (Dodson 1973) when using argon geochronological data to constrain temperature–time paths in orogenic settings. The closure temperature (T_c) concept originally formulated by Dodson (1973) is based on the assumption that a sample has undergone slow cooling (linear in 1/T) from temperatures high enough to prevent the accumulation of a radiogenic daughter product (for example $^{40}Ar^*$) within a given mineral, to temperatures low enough such that the radiogenic daughter product is quantitatively retained. Between these extreme states there is a continuous

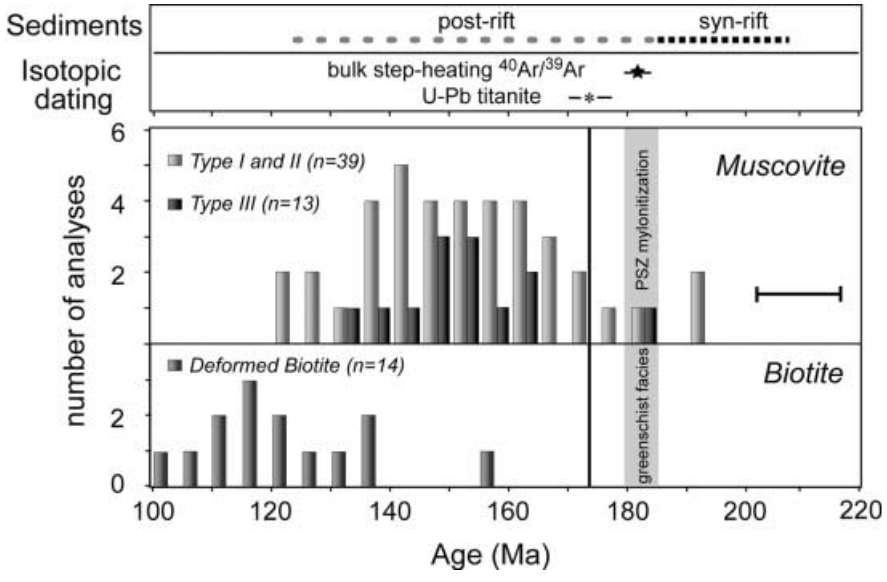

Fig. 5 Sedimentary and isotopic age constraints for Pogallo mylonitization combined with a histogram of in-situ $^{40}Ar/^{39}Ar$ UV-laser ablation analyses for muscovite and biotite. The 2σ error for individual laser analyses is given for reference. The *shaded area* marks the age of greenschist facies mylonitization along the Pogallo Shear Zone as constrained by $^{40}Ar/^{39}Ar$ furnace step-heating of foliation-forming type I muscovite porphyroclasts. *Black asterisk* with *2σ error bars* indicates the formation age of metamorphic titanite in the IVZ at 173 ± 4 Ma. Late Norian to early Toarcian rifting involved deposition of breccias, sandstones and siliceous limestones in half grabens related to Pogallo mylonitization at depth. Toarcian to Early Cretaceous post-rifting thermal subsidence is marked by deposition of pelagic limestones and radiolarites

transition over which the loss of radiogenic daughter product is first balanced, then exceeded by its accumulation within a mineral (Fig. 7). For thermally activated diffusion, the closure temperature is a function of material properties (i.e. activation energy and diffusion coefficient), the time over which the transition in daughter accumulation occurs (governed by the cooling rate) and the effective diffusion dimension, which is often assumed to be equivalent to the grain radius. Although it is common in thermochronological studies to assign a specific isotopic closure temperature to given minerals for calculating temperature–time paths there is no unique 'closure temperature' for any particular mineral. This is simply because natural materials exhibit a large range in effective diffusion length scale and diffusion characteristics.

The coexistence of strongly deformed muscovite with early syn-kinematic fibrolitic sillimanite and biotite indicates that the Pogallo mylonites experienced temperatures of about 500 °C prior to and/or during the initial stages of mylonitization. This temperature estimate is consistent with a value of 430 ± 40 °C obtained from the quartz and muscovite oxygen isotope data. Deformation temperatures obtained by oxygen isotope thermometry are higher than the estimated argon closure temperature of 380–400 °C for muscovite in the Pogallo mylonites [calculated for the observed, average grain size of 500–750 μm at right angles to the *xz*-fabric plane (type I grains), a cooling rate of 2 °C/Ma, activation energy of 55 kcal/mol, and a pre-exponential factor of 0.24 cm^2/s Kirschner et al. 1996]. Considered in the context of independent structural, sedimentological and geochronological evidence, the in-situ $^{40}Ar/^{39}Ar$ data reported here cannot be regarded as formational ages. Rather, the $^{40}Ar/^{39}Ar$ ages record either post-mylonitic re-heating above or close to the closure temperature to argon diffusion, disturbance of the $^{40}Ar/^{39}Ar$ system during post-mylonitic reworking of the fault zone or slow post-mylonitic cooling over several tens of millions of years.

The first interpretation, a post-mylonitic thermal overprint, is highly unlikely as there is no microstruc-

Table 2 Step-heating $^{40}Ar/^{39}Ar$ analyses of muscovite from micaceous mylonite of the Pogallo Shear Zone. Data corrected for system blanks, radioactive decay subsequent to irradiation, mass discrimination and interfering K-, Ca-, and Cl-derived isotopes of argon

Sample no.	^{40}Ar ($\times10^{-13}$ mol)	^{39}Ar ($\times10^{-14}$ mol)	^{38}Ar ($\times10^{-16}$ mol)	^{36}Ar ($\times10^{-16}$ mol)	$^{37}Ar/^{39}Ar$	$^{40}Ar^*/^{39}Ar$	$\%^{40}Ar^*$	Date (Ma ± 2σ)
20UL-28 undeformed								
850	1.9969 ± 0.3385	0.7721 ± 0.1327	1.1229 ± 0.2190	0.6202 ± 0.0889	–	23.41	90.8	185.7 ± 2.8
875	2.5423 ± 0.3457	1.0085 ± 0.1358	1.5413 ± 0.2355	0.7581 ± 0.0930	0.0118	22.91	91.2	181.9 ± 2.6
900	3.9498 ± 0.3548	1.5609 ± 0.1393	2.2808 ± 0.2289	1.0322 ± 0.0927	0.0082	23.27	92.3	184.6 ± 2.6
925	8.6854 ± 0.3652	3.4322 ± 0.1435	4.9659 ± 0.2373	2.3363 ± 0.0958	0.0032	23.22	92.0	184.2 ± 2.6
950	12.2920 ± 0.3764	5.0239 ± 0.1477	6.7256 ± 0.3724	2.1726 ± 0.0990	0.0039	23.11	94.8	183.4 ± 2.6
976	18.4273 ± 0.3883	7.7562 ± 0.1524	10.3916 ± 0.2723	1.8272 ± 0.1014	0.0012	22.98	97.1	182.4 ± 2.6
1000	13.2567 ± 0.3992	5.6614 ± 0.1566	7.4193 ± 0.5389	0.9948 ± 0.1048	0.0008	22.82	97.8	181.2 ± 2.6
1050	12.3684 ± 0.4172	5.1731 ± 0.1639	6.9636 ± 0.5275	1.9055 ± 0.1099	0.0022	22.74	95.4	180.6 ± 2.6
1100	10.5153 ± 0.4269	4.3108 ± 0.1675	5.9798 ± 0.4690	2.3792 ± 0.1117	0.0024	22.69	93.3	180.2 ± 2.6
1150	6.7997 ± 0.4250	2.6343 ± 0.1665	3.8449 ± 0.3174	2.5070 ± 0.1107	0.0022	22.92	89.1	182.0 ± 2.6
1250	6.6015 ± 0.3884	2.1131 ± 0.1525	3.8695 ± 0.4559	5.9027 ± 0.1028	0.0087	22.91	73.5	181.9 ± 2.8
1350	12.1615 ± 0.3897	4.2318 ± 0.1528	7.0787 ± 0.5633	8.4678 ± 0.1038	0.0023	22.75	79.4	180.7 ± 2.8
Weight = 8.25 mg, J value = 0.00463								
20UL-25 undeformed								
700	1.9453 ± 0.0038	0.0996 ± 0.0003	1.6201 ± 0.0417	5.8345 ± 0.0144	5.9623	23.04	11.6	182.8 ± 19.0
750	1.0375 ± 0.0021	0.1538 ± 0.0004	0.5407 ± 0.0152	2.3010 ± 0.0109	1.1111	23.35	34.5	185.2 ± 5.6
800	1.0728 ± 0.0024	0.2856 ± 0.0005	0.4870 ± 0.0297	1.2829 ± 0.0106	0.1307	24.23	64.6	191.8 ± 3.2
850	9.5058 ± 0.0165	3.6876 ± 0.0056	4.6601 ± 0.1449	3.2452 ± 0.0115	–	23.10	89.9	183.3 ± 2.6
875	4.0181 ± 0.0055	1.6483 ± 0.0018	2.1487 ± 0.1317	0.7818 ± 0.0103	–	22.90	94.2	181.8 ± 2.6
900	2.1562 ± 0.0030	0.8662 ± 0.0011	0.9449 ± 0.0345	0.5715 ± 0.0101	–	22.87	92.1	181.6 ± 2.6
950	1.9958 ± 0.0059	0.7562 ± 0.0015	1.2978 ± 0.1104	0.9771 ± 0.0164	–	22.54	85.5	179.1 ± 3.2
1000	1.5726 ± 0.0021	0.5417 ± 0.0004	0.7206 ± 0.0465	1.0100 ± 0.0108	–	23.45	81.0	185.9 ± 2.8
1050	1.8185 ± 0.0022	0.6238 ± 0.0004	0.8336 ± 0.0512	1.1881 ± 0.0110	–	23.45	80.6	185.9 ± 2.8
1100	3.1677 ± 0.0077	1.2631 ± 0.0024	1.6137 ± 0.0850	0.8516 ± 0.0120	–	23.01	92.0	182.6 ± 2.6
1200	1.2327 ± 0.0027	0.4881 ± 0.0005	0.4778 ± 0.0424	0.2788 ± 0.0131	–	23.49	93.3	186.3 ± 2.6
Weight = 1.55 mg, J value = 0.00463								
20UL-27 (strongly deformed)								
800	1.5210 ± 0.1359	1.3879 ± 0.0171	0.2171 ± 0.1218	0.1745 ± 0.1891	–	10.51	96.6	85.7 ± 1.4
900	4.8657 ± 0.1359	2.7520 ± 0.0171	1.6323 ± 0.3066	0.8928 ± 0.1922	–	16.64	94.6	133.9 ± 2.0
1000	10.0216 ± 0.1359	4.9498 ± 0.0173	4.2060 ± 0.4409	1.1555 ± 0.1896	–	19.48	96.6	155.8 ± 2.2
1100	21.4867 ± 0.1360	9.9242 ± 0.0180	10.9410 ± 0.8023	1.2264 ± 0.1896	–	21.21	98.3	169.0 ± 2.4
1150	13.9939 ± 0.1358	6.6621 ± 0.0173	6.8065 ± 0.1544	1.5550 ± 0.1935	–	20.24	96.7	161.6 ± 2.4
1200	9.6856 ± 0.1359	4.8650 ± 0.0173	4.4023 ± 0.4653	0.8213 ± 0.1963	–	19.33	97.5	154.7 ± 2.2
1250	9.7635 ± 0.1358	4.4904 ± 0.0172	4.3611 ± 0.4478	2.9347 ± 0.1901	–	19.73	91.1	157.7 ± 2.2
1300	28.2876 ± 0.1360	10.1450 ± 0.0177	16.0010 ± 0.7013	17.3883 ± 0.1924	–	22.74	81.8	180.6 ± 2.6
Weight = 8.44 mg, J value = 0.00463								

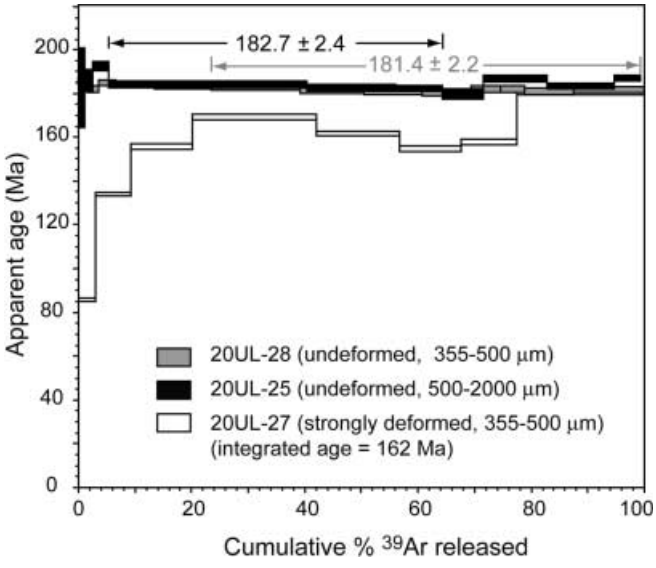

Fig. 6 Furnace step-heating spectra of undeformed and deformed type I muscovite porphyroclasts of the investigated sample. Strongly deformed and kinked type I muscovite grains (20UL-27) produce a staircase $^{40}Ar/^{39}Ar$ spectrum consistent with significant argon loss. Individual steps record the same range of ages observed in the in-situ UV-laser experiments

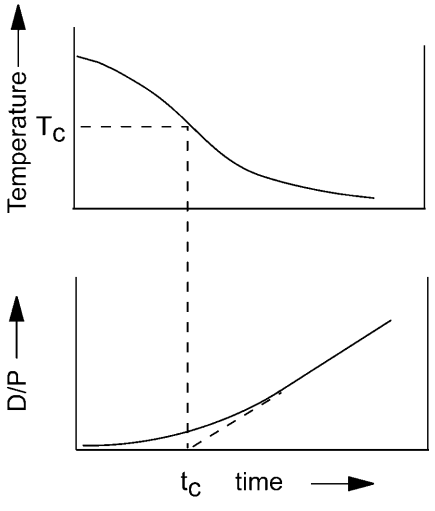

Fig. 7 Plot of temperature and daughter to parent ratio (D/P) versus time from Dodson (1973). Note that, although closure temperature (T_c) approximates the time (t_c) of total daughter retention, the time interval of partial daughter retention is recorded in this investigation

tural evidence of post-tectonic annealing in any of the minerals within the sample. Experimentally determined grain boundary migration rates in quartz are rapid above 300–320 °C (Masuda et al. 1997), so the lack of static recrystallization in quartz in the mylonite (Fig. 2c) points to rapid cooling below this critical temperature at the end of mylonitization. The transition from dislocation creep to brittle fracture and cataclastic flow in quartzose rocks occurs at about 300–350 °C at geological strain rates (e.g. Sibson 1977). Taken together, these

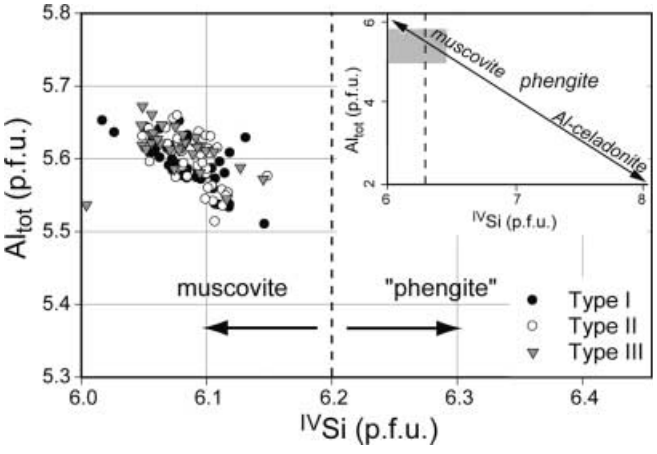

Fig. 8 Electron microprobe analyses of the three microstructurally distinct types of muscovite within the Pogallo mylonites plotted in co-ordinates of Al_{tot} and Si^{IV} (muscovite composition normalized to 12 small cations). All three types plot within the muscovite field and show a very restricted range in composition. Muscovite definition after IMA Mica Subcommittee (Rieder et al. 1999)

data indicate that the temperature in the southern Alpine basement never exceeded 300 °C since the end of rift-related mylonitization. We can also rule out that the inter- and intra-grain variability of $^{40}Ar/^{39}Ar$ apparent ages is the result of brittle reworking or fluid alteration during a later, previously unrecognized (e.g. Alpine) tectonic event. The lack of brittle deformation structures at both the outcrop and thin-section scale, and the complete absence of fluid-mediated mineral alteration within the syn-mylonitic paragenesis as observed in thin section and documented by very homogeneous mica compositions (Fig. 8), strongly discounts such a scenario. Any process evoked to explain the results of this study has to account for the marked intra- and inter-grain variability of $^{40}Ar/^{39}Ar$ apparent ages. As has been shown recently by $^{40}Ar/^{39}Ar$ dating of experimentally deformed white mica (Dunlap and Kronenberg 2001), low-temperature cataclastic deformation even at high finite strains is unable to produce measurable changes in $^{40}Ar/^{39}Ar$ ratios and is, therefore, unable to produce the heterogeneous apparent age patterns observed within type I porphyroclasts.

Inter- and intra-grain variations in $^{40}Ar^*$ within strongly deformed muscovite porphyroclasts

A variety of factors could lead to the observed intra-grain variation of in-situ $^{40}Ar/^{39}Ar$ dates in type I porphyroclasts (Fig. 4) including: (1) 'contamination' of the analysed porphyroclasts by inclusions of other mineral phases or relict muscovite crystals; (2) incorporation of excess argon from external reservoirs during or after deformation; (3) lack of pervasive isotopic homogenization of isotopically heterogeneous muscovite during metamorphism associated with Pogallo mylonitization;

and (4) retention of $^{40}Ar^*$ diffusive-loss gradients that developed during the post-deformational history.

1. Contamination by inclusions or relict muscovite grains. The diffusion kinetics of argon within the mica lattice can be controlled by ionic porosity (Dahl 1996). The ionic porosity model incorporates variations in major and minor element chemistry, lattice defects and vacancies, which are all important variables that affect the interlayer bond length in a mica lattice. Therefore, chemically zoned grains (or grain populations) may contain heterogeneous argon compositions because of zonation induced by recrystallization and re-equilibration with its environment (Giorgis et al. 2000) or because of chemically diverse zones of the grain having different retention properties (Villa et al. 1996). Inherited relict grains that escaped deformation and were not completely reset during the early high temperature stages of Pogallo mylonitization could be the source of an older $^{40}Ar^*$ component. In this case, the in-situ UV-laser data and the plateau-forming spectra would reflect a mixture of different argon reservoirs and hence give a meaningless 'mixed age'. Clearly, the remarkable intra- and inter-grain compositional homogeneity of type I muscovites determined by electron microprobe analyses (Table 1 and Fig. 8) is inconsistent with such an explanation for the observed age variability. Chlorine-rich fluid inclusions are also known to be hosts for excess ^{40}Ar (e.g. Harrison et al. 1994) and could be evoked for the heterogeneous age pattern in type I porphyroclasts. However, detailed microprobe investigations again failed to detect either Cl or Ca as possible contaminants, and there is no positive correlation between apparent age and Ca-derived ^{37}Ar or Cl-derived ^{38}Ar. Consequently, the oldest in-situ UV-laser ages in the strongly deformed porphyroclasts, which overlap within error with the plateau ages of the undeformed muscovite (Fig. 5), are not artefacts of relict grains or influenced by secondary mineral phases, but most likely record the same event as the undeformed grains.
2. Heterogeneous incorporation of excess argon into deformed muscovite grains. In-situ UV-laser traverses across strongly deformed type I porphyroclasts were made to investigate the intra-grain spatial distribution of $^{40}Ar^*$. This involved the analysis of core and rim compositions. As shown in Fig. 4, there is no systematic correlation between position of the laser pit within the grain and argon isotope ratios. In-situ analyses of fine-grained quartz–biotite mixtures in C′ shear bands (e.g. 15UL-5.3 in Table 3) document excess argon. Heterogeneous uptake of this excess argon into marginal parts of the grain or along microfractures would generally result in significantly older apparent ages. Yet, exactly the opposite is observed in muscovite from the Pogallo mylonites. Independent geological evidence and the results of furnace $^{40}Ar/^{39}Ar$ step-heating clearly demonstrate that most of the in-situ ages are too young to date the actual age of mylonitization along the PSZ and only the oldest apparent ages within strongly deformed porphyroclasts overlap within error with the actual age of deformation (Fig. 5), thus eliminating excess argon as a significant influence for the observed ages.
3. Although we cannot directly determine the initial $^{40}Ar/^{36}Ar$ ratio, a highly variable initial $^{40}Ar/^{36}Ar$ ratio appears to be a rather unlikely explanation for the range of apparent ages. The in-situ analyses for type I muscovites when plotted on an isochron diagram yield an apparent age of 145 ± 5.4 Ma with a $^{40}Ar/^{36}Ar$ intercept of 291 ± 29 (MSWD = 1.5), both well within the error-weighted average for type I grains (147.7 ± 5.1 Ma) and the present day atmospheric $^{40}Ar/^{36}Ar$ value of 295.5, respectively.

A model of microstructurally controlled diffusion segments

By establishing that mica composition does not influence our $^{40}Ar/^{39}Ar$ data, the results of in-situ $^{40}Ar/^{39}Ar$ dating from strongly deformed porphyroclasts offer considerable potential for furthering our understanding of argon loss in deformed muscovite. The most convincing interpretation for the variable in-situ $^{40}Ar/^{39}Ar$ data is that muscovites from the Pogallo mylonites were subject to post-mylonitic diffusional argon loss. However, volume diffusion assuming a single diffusion length scale (e.g. the grain scale or a fixed fraction thereof) cannot explain the pattern of intra-grain $^{40}Ar/^{39}Ar$ age variations and the age difference between deformed and undeformed grains obtained by in-situ UV-laser ablation and furnace step-heating. Interestingly, the complicated pattern of microstructures for muscovite from the PSZ is consistent with argon diffusing from heterogeneously-sized coherent segments (Fig 2a, d) into zones with high defect density (high- and low-angle kink bands, zones of undulatory extinction, and discrete intragranular microfractures). These defect sites commonly occur at high angles to the K-interlayer and provided fast diffusion pathways (Lee 1993, 1995; Villa 1994), which facilitated argon transport to grain boundaries. Diffusional transport of $^{40}Ar^*$ can only be efficient if the concentration gradients are favourable. In-situ analyses of fine-grained biotite shear bands display erroneously old apparent ages consistent with a net transport of $^{40}Ar^*$ to zones of recrystallization and mineral formation. The presence of measurable excess argon within mylonitic quartz–biotite shear bands (e.g. 15UL-5.5 in Table 3) suggests that recrystallized quartz was acting as a sink or reservoir for excess ^{40}Ar. The high mobility of quartz grain boundaries in a dynamically deforming quartz matrix supposedly enhances argon transport within the mylonitic rock and hence the incremental argon concentration at the outside of the muscovite grains approaches zero, a

Table 3 In-situ $^{40}Ar/^{39}Ar$ analyses of muscovite and biotite from micaceous mylonite of the Pogallo Shear Zone. Data corrected for system blanks, radioactive decay subsequent to irradiation, mass discrimination and interfering K-, Ca- and Cl-derived isotopes of argon

Sample no.	^{40}Ar ($\times10^{-15}$ mol)	^{39}Ar ($\times10^{-16}$ mol)	^{38}Ar ($\times10^{-17}$ mol)	^{37}Ar ($\times10^{-16}$ mol)	^{36}Ar ($\times10^{-17}$ mol)	$^{40}Ar^*/^{39}Ar$	$\%^{40}Ar^*$	Date (Ma $\pm 2\sigma$)
Type I and II muscovite								
15UL-1.15	1.7333 ± 0.0028	0.9803 ± 0.0064	0.225 ± 0.027	–	0.2653 ± 0.0085	9.69	54.8	168.1 ± 5.0
15UL-1.16	0.8059 ± 0.0036	0.6348 ± 0.0043	0.116 ± 0.016	–	0.0808 ± 0.0086	8.93	70.4	155.5 ± 6.4
15UL-1.17	0.9681 ± 0.0045	0.7452 ± 0.0044	0.118 ± 0.024	–	0.0917 ± 0.0075	9.35	72.0	162.5 ± 4.8
15UL-1.18	0.7178 ± 0.0035	0.5742 ± 0.0047	0.119 ± 0.018	–	0.0886 ± 0.0085	7.94	63.5	138.9 ± 6.8
15UL-1.19	0.8907 ± 0.0033	0.7425 ± 0.0040	0.142 ± 0.023	0.110 ± 0.109	0.0644 ± 0.0078	9.44	78.7	164.0 ± 5.2
15UL-2.1	0.9533 ± 0.0045	0.7762 ± 0.0053	0.114 ± 0.014	–	0.0808 ± 0.0083	9.20	74.9	160.0 ± 4.6
15UL-2.2	0.5706 ± 0.0029	0.4702 ± 0.0030	0.056 ± 0.013	–	0.0528 ± 0.0070	8.81	72.6	153.4 ± 7.4
15UL-2.3	0.6388 ± 0.0027	0.5402 ± 0.0030	0.080 ± 0.012	–	0.0503 ± 0.0088	9.07	76.7	157.8 ± 5.4
15UL-2.4	0.5239 ± 0.0027	0.4365 ± 0.0038	0.046 ± 0.014	–	0.0178 ± 0.0097	10.79	89.9	186.3 ± 6.0
15UL-2.5	0.6783 ± 0.0026	0.5262 ± 0.0037	0.077 ± 0.015	0.399 ± 0.094	0.0924 ± 0.0088	7.76	60.2	135.9 ± 8.4
15UL-2.6	0.6754 ± 0.0030	0.5654 ± 0.0045	0.073 ± 0.014	–	0.0734 ± 0.0088	8.10	67.9	141.7 ± 5.8
15UL-2.7	0.6574 ± 0.0035	0.5609 ± 0.0051	0.067 ± 0.014	0.424 ± 0.118	0.0573 ± 0.0083	8.76	74.7	152.6 ± 6.8
15UL-2.8	0.4322 ± 0.0022	0.3359 ± 0.0034	0.065 ± 0.012	–	0.0213 ± 0.0092	10.99	85.4	189.5 ± 11.1
15UL-2.9	0.3378 ± 0.0016	0.1090 ± 0.0022	0.033 ± 0.014	–	0.0182 ± 0.0055	26.06	84.1	420.8 ± 11.1
15UL-2.11	0.5837 ± 0.0027	0.5010 ± 0.0036	0.111 ± 0.018	0.289 ± 0.127	0.0835 ± 0.0075	6.77	58.1	119.1 ± 7.2
15UL-2.12	0.7781 ± 0.0031	0.6851 ± 0.0042	0.139 ± 0.016	–	0.1005 ± 0.0086	7.03	61.9	123.4 ± 6.0
15UL-2.13	0.8409 ± 0.0030	0.7174 ± 0.0040	0.159 ± 0.015	–	0.1011 ± 0.0081	7.55	64.5	132.4 ± 5.2
15UL-2.17	1.1749 ± 0.0034	1.0117 ± 0.0057	0.212 ± 0.022	–	0.1341 ± 0.0084	7.69	66.3	134.7 ± 3.8
15UL-2.18	1.0778 ± 0.0023	0.9401 ± 0.0060	0.203 ± 0.021	–	0.1405 ± 0.0084	7.05	61.5	123.8 ± 4.6
15UL-2.19	1.1884 ± 0.0042	1.0676 ± 0.0055	0.243 ± 0.022	–	0.1083 ± 0.0083	8.13	73.1	142.1 ± 3.6
15UL-2.20	1.0229 ± 0.0017	0.9062 ± 0.0054	0.177 ± 0.017	–	0.1090 ± 0.0077	7.73	68.5	135.3 ± 4.2
15UL-2.21	1.0597 ± 0.0026	0.9492 ± 0.0051	0.147 ± 0.015	–	0.0873 ± 0.0077	8.44	75.6	147.3 ± 4.6
15UL-2.22	1.0653 ± 0.0029	0.9418 ± 0.0052	0.153 ± 0.022	–	0.0980 ± 0.0077	8.23	72.8	143.8 ± 4.2
15UL-2.23	1.1700 ± 0.0020	1.0297 ± 0.0055	0.174 ± 0.020	0.229 ± 0.131	0.1221 ± 0.0086	7.87	69.3	137.7 ± 4.6
15UL-2.24	1.0844 ± 0.0019	0.9581 ± 0.0050	0.165 ± 0.016	0.113 ± 0.100	0.1219 ± 0.0083	7.56	66.8	132.5 ± 4.2
15UL-2.25	1.0881 ± 0.0024	0.9770 ± 0.0044	0.203 ± 0.014	–	0.1144 ± 0.0074	7.67	68.9	134.4 ± 4.0
15UL-2.26	1.1801 ± 0.0020	1.0313 ± 0.0055	0.134 ± 0.019	0.165 ± 0.163	0.1118 ± 0.0089	8.25	72.1	144.0 ± 3.8
15UL-3.1	0.8904 ± 0.0021	0.7220 ± 0.0052	0.115 ± 0.019	–	0.0504 ± 0.0067	10.27	83.3	177.7 ± 4.8
15UL-3.2	0.7904 ± 0.0022	0.6761 ± 0.0030	0.120 ± 0.017	–	0.0702 ± 0.0086	8.62	73.7	150.3 ± 6.0
15UL-3.3	0.8328 ± 0.0024	0.6487 ± 0.0034	0.112 ± 0.018	–	0.0738 ± 0.0096	9.47	73.8	164.4 ± 5.4
15UL-3.4	0.7602 ± 0.0016	0.6077 ± 0.0047	0.151 ± 0.016	–	0.0814 ± 0.0077	8.55	68.4	149.1 ± 5.0
15UL-3.5	0.7351 ± 0.0017	0.6266 ± 0.0036	0.097 ± 0.011	–	0.0618 ± 0.0078	8.81	75.1	153.5 ± 6.2
15UL-3.6	0.6328 ± 0.0014	0.4945 ± 0.0037	0.099 ± 0.019	–	0.0653 ± 0.0079	8.90	69.6	155.0 ± 6.6
15UL-3.7	0.6584 ± 0.0014	0.4572 ± 0.0031	0.101 ± 0.014	–	0.0730 ± 0.0082	9.68	67.2	167.9 ± 7.4
15UL-4.2	0.6819 ± 0.0018	0.5951 ± 0.0030	0.043 ± 0.013	0.191 ± 0.084	0.0715 ± 0.0075	7.93	69.2	138.7 ± 6.0
15UL-4.3	0.6536 ± 0.0014	0.5793 ± 0.0043	0.034 ± 0.012	0.363 ± 0.094	0.0792 ± 0.0072	7.29	64.6	127.9 ± 5.8
15UL-4.4	0.5890 ± 0.0017	0.4930 ± 0.0029	0.044 ± 0.012	0.601 ± 0.123	0.0902 ± 0.0074	6.64	55.5	116.8 ± 7.4
15UL-4.5	0.5121 ± 0.0016	0.4437 ± 0.0028	0.039 ± 0.008	–	0.0232 ± 0.0070	10.01	86.8	173.4 ± 6.0
15UL-5.1	0.7504 ± 0.0015	0.6499 ± 0.0044	0.109 ± 0.015	–	0.0665 ± 0.0087	8.53	73.8	148.8 ± 5.6
15UL-5.2	0.6709 ± 0.0020	0.5910 ± 0.0036	0.121 ± 0.019	–	0.0607 ± 0.0070	8.31	73.2	145.1 ± 5.8
Type III muscovite								
15UL-3.9	1.0457 ± 0.0039	0.8610 ± 0.0043	0.098 ± 0.021	–	0.1149 ± 0.0078	8.19	67.5	143.2 ± 4.2
15UL-3.10	0.8257 ± 0.0028	0.6530 ± 0.0042	0.095 ± 0.013	–	0.0930 ± 0.0073	8.44	66.7	147.2 ± 5.0
15UL-3.11	1.0502 ± 0.0026	0.9030 ± 0.0051	0.119 ± 0.025	–	0.0831 ± 0.0064	8.91	76.6	155.1 ± 3.6
15UL-3.12	0.9259 ± 0.0020	0.8196 ± 0.0037	0.103 ± 0.016	–	0.0775 ± 0.0069	8.50	75.2	148.2 ± 4.0
15UL-3.13	1.0012 ± 0.0025	0.8278 ± 0.0057	0.026 ± 0.013	–	0.0548 ± 0.0070	10.13	83.8	175.4 ± 4.4
15UL-3.16	0.9465 ± 0.0024	0.8623 ± 0.0045	0.114 ± 0.021	–	0.0797 ± 0.0086	8.25	75.2	144.0 ± 4.6
15UL-3.17	0.7731 ± 0.0017	0.6714 ± 0.0048	0.137 ± 0.017	0.091 ± 0.074	0.0966 ± 0.0084	7.27	63.2	127.6 ± 5.2
15UL-4.9	1.1413 ± 0.0020	0.9964 ± 0.0048	0.146 ± 0.015	0.111 ± 0.057	0.1047 ± 0.0076	8.35	73.0	145.9 ± 3.6
15UL-4.10	1.0520 ± 0.0023	0.8634 ± 0.0048	0.184 ± 0.016	0.230 ± 0.106	0.0964 ± 0.0070	8.90	73.1	155.0 ± 3.8
15UL-4.11	1.1769 ± 0.0022	1.0457 ± 0.0056	0.186 ± 0.018	0.153 ± 0.088	0.1267 ± 0.0087	7.68	68.3	134.5 ± 3.6
15UL-4.12	1.0336 ± 0.0017	0.8857 ± 0.0054	0.198 ± 0.026	0.212 ± 0.084	0.1065 ± 0.0075	8.13	69.7	142.1 ± 4.6
15UL-4.13	1.0411 ± 0.0018	0.9048 ± 0.0051	0.180 ± 0.014	0.196 ± 0.101	0.1143 ± 0.0080	7.79	67.7	136.3 ± 4.8
15UL-4.19	0.7738 ± 0.0019	0.6741 ± 0.0044	0.110 ± 0.019	–	0.0596 ± 0.0079	8.86	77.2	154.4 ± 4.2
Deformed biotite								
15UL-1.3	1.3613 ± 0.0032	1.1592 ± 0.0058	0.261 ± 0.025	–	0.2041 ± 0.0096	6.54	55.7	115.1 ± 3.8
15UL-1.4	1.3657 ± 0.0026	1.1481 ± 0.0061	0.263 ± 0.022	–	0.2044 ± 0.0083	6.63	55.8	116.7 ± 4.2
15UL-1.5	1.2795 ± 0.0035	1.0527 ± 0.0059	0.245 ± 0.022	–	0.2111 ± 0.0080	6.22	51.2	109.8 ± 4.0
15UL-1.6	1.3343 ± 0.0038	1.1897 ± 0.0082	0.316 ± 0.020	–	0.1755 ± 0.0080	6.85	61.1	120.5 ± 4.0
15UL-1.7	1.2915 ± 0.0038	1.1408 ± 0.0056	0.288 ± 0.023	–	0.1765 ± 0.0080	6.75	59.6	118.7 ± 4.0
15UL-1.8	1.3943 ± 0.0126	1.2364 ± 0.0099	0.288 ± 0.021	–	0.1825 ± 0.0087	6.91	61.3	121.5 ± 4.8
15UL-1.9	1.3123 ± 0.0038	1.1223 ± 0.0043	0.266 ± 0.025	–	0.1423 ± 0.0081	7.94	68.0	138.9 ± 3.8
15UL-1.10	1.2861 ± 0.0041	1.1112 ± 0.0058	0.297 ± 0.018	–	0.1428 ± 0.0076	7.77	67.2	136.1 ± 3.6

Table 3 (Contd.)

Sample no.	^{40}Ar ($\times10^{-15}$ mol)	^{39}Ar ($\times10^{-16}$ mol)	^{38}Ar ($\times10^{-17}$ mol)	^{37}Ar ($\times10^{-16}$ mol)	^{36}Ar ($\times10^{-17}$ mol)	^{40}Ar*/^{39}Ar	%^{40}Ar*	Date (Ma $\pm 2\sigma$)
15UL-1.11	1.2321 ± 0.0046	1.0495 ± 0.0063	0.146 ± 0.020	–	0.1467 ± 0.0079	7.60	64.8	133.2 ± 4.4
15UL-1.13	1.0937 ± 0.0038	0.9244 ± 0.0053	0.157 ± 0.018	0.181 ± 0.106	0.1669 ± 0.0084	6.51	55.0	114.6 ± 4.4
15UL-1.14	1.0349 ± 0.0042	0.9483 ± 0.0056	0.114 ± 0.018	0.109 ± 0.075	0.1495 ± 0.0091	6.26	57.4	110.4 ± 5.2
15UL-4.14	0.5660 ± 0.0022	0.5238 ± 0.0042	0.319 ± 0.017	–	0.0304 ± 0.0090	9.09	84.1	158.1 ± 6.0
15UL-4.17	0.5443 ± 0.0013	0.4725 ± 0.0044	0.152 ± 0.020	–	0.0899 ± 0.0089	5.90	51.2	104.2 ± 8.4
15UL-4.18	0.6340 ± 0.0018	0.5271 ± 0.0040	0.106 ± 0.021	–	0.8608 ± 0.0093	7.20	59.9	126.4 ± 7.0
Recrystallized biotite and quartz in shear bands								
15UL-SP5.3	1.0730 ± 0.0034	0.2017 ± 0.0026	0.064 ± 0.012	–	0.0832 ± 0.0081	40.99	77.1	623.9 ± 7.0
15UL-SP5.5	1.0848 ± 0.0027	0.0443 ± 0.0030	0.065 ± 0.012	0.235 ± 0.934	0.1223 ± 0.0092	164.42	66.8	1763.1 ± 27.64
15UL-SP5.12	1.9547 ± 0.0044	0.1213 ± 0.0027	0.074 ± 0.019	–	0.1830 ± 0.0093	116.53	72.3	1401.5 ± 13.01

prerequisite in the model of Dodson (1973). Therefore, we propose that deformational microstructures and zones of high dislocation/defect density that connect coherent internal domains (to which we refer as 'microstructurally controlled diffusion segments') with the external surface of the grain play an important role in controlling the diffusion and concentration of ^{40}Ar*. Crystal plastic deformation of the Pogallo muscovites induced heterogeneous segmentation of individual grains, with each segment bounded by zones of high defect density or intragranular microfractures (Fig. 2d). Such lattice defects form the boundaries of microstructurally controlled diffusion segments and reduce the physical (observed) grain size and, hence, the characteristic length scale for argon diffusion. This conclusion is consistent with the results of Dunlap and Kronenberg (2001) who speculated that grain segmentation affects the ability to retain argon in micas deformed under laboratory conditions.

There are different reasons to assume that ^{40}Ar* will migrate preferably towards zones of high dislocation density. Radiogenic ^{40}Ar* (1.9 Å) produced by in-situ decay of ^{40}K does not fit into the K^+ (1.33 Å) sites and, therefore, acts as an 'impurity' in the mineral lattice. Impurities, however, are known to create lattice distortions that are partially released once the impurity has changed its intracrystalline position. Hence, an argon atom will migrate to sites where its potential energy is lowered considerably, such as defect sites in the crystal lattice (Lee 1995). There are currently no experimental data in the earth science literature for noble gas behaviour in strained solids. In materials science, however, Blavette et al. (1999) used 3-D atomic-scale imaging to establish that, in boron-doped Fe–Al-alloys, the boron 'impurities' are enriched by a factor of 50 along edge dislocations. Moreover, it is well known from a number of materials that stress-induced migration of diffusing species leads to their segregation along dislocation lines and hence to an enrichment of the diffusing species at deformed lattice sites. Application of these results to natural minerals might not be straightforward, but, nevertheless, they serve as a qualitative guide to interpreting the observations made in this study.

If zones of high-dislocation density in a highly strained muscovite are associated with first-order lattice discontinuities, such as microfractures or zones of high-angle kink bands (Fig. 2d, e), diffusive argon loss is more strongly controlled by these segment-bounding discontinuities than by volume diffusion on the grain scale. As 'closure temperature' (Dodson 1973) is partly a function of a^2 (i.e. the square of the diffusion length scale), any reduction in that variable will lower the closure temperature of a given mineral. Introducing a large number of heterogeneously spaced and sized segments separated by zones of high defect density (i.e. fast diffusion pathways) into the mica lattice will significantly affect its overall argon retentivity (see also Reddy and Potts 1999). Therefore, the formation of microstructurally controlled diffusion segments inevitably results in variable closure temperatures for each segment and hence a range of cooling ages within individual grains. Indeed, for rocks with sufficiently slow cooling rates, this model predicts that a heterogeneous age distribution should be observed in analysed grains that have the above-mentioned microstructures. Moreover, in a mechanically strongly anisotropic mineral such as muscovite, where microstructures are heterogeneously distributed at the grain scale (Fig. 2a, d, e), the spatial resolution of the UV-laser probe provides a powerful tool for directly imaging the influence of microstructures on argon isotopes. Such predicted age variability on the intra-grain scale is observed in the strongly deformed muscovite of the Pogallo mylonites. In these samples, because microstructurally controlled diffusion segments are unevenly distributed, apparent age variations observed in transects across individual grains directly reflect the microstructural heterogeneity and its influence on diffusional argon loss. In-situ UV-laser traverses at high angles to {001} display both highly variable apparent ages (Fig. 4, traverses A and B) and extremely young apparent ages in seemingly 'pristine' parts (Fig. 4, traverse C) of a type I porphyroclast. These observations are consistent with analyses of variably sized segments either in the terminations of individual grains (Fig. 2e) or coherent but narrow segments that transect entire grains at high angles to {001} (Fig. 2a, d). Such age variability has recently been observed in other slowly

cooled high-grade metamorphic rocks (Janak et al. 2001).

The model of argon loss via microstructurally controlled diffusion segments explains the apparent contradiction that error-weighted averages of in-situ $^{40}Ar/^{39}Ar$ data for types I and III are analytically indistinguishable (147.7 ± 5.1 vs 147.3 ± 6.5 Ma) even though their observed grain size differs by at least one order of magnitude. Available geochronological data for the IVZ indicate slow post-mylonitic cooling of 1–2 °C/Ma after Pogallo mylonitization had ceased (Handy and Zingg 1991; Hunziker et al. 1992). Slow cooling will accentuate the effects of thermally controlled volume diffusion. If the effective length scale for argon diffusion in deformed muscovite was the grain radius, and volume diffusion the active mechanism, one would expect to see a shift to consistently younger apparent ages within the much smaller type III muscovites. It is obvious from Fig. 5 that this is not the case. Because the in-situ analyses of type III grains occupy the same age range as type I and also yield highly variable $^{40}Ar/^{39}Ar$ apparent ages, the effective diffusion length scale has to be controlled by intra-grain microstructures that are found in both microstructurally distinct types. The model of microstructurally controlled segments, therefore, envisages volume diffusion on the segment scale, rapid argon transport within first-order lattice discontinuities described above, and successive closure with decreasing size of individual intra-grain segments to argon diffusion over a time span of about 60 million years.

Interestingly, there are no reliable isotopic ages available between 170–180 Ma (K–Ar muscovite) and 60–70 Ma (zircon fission track) to constrain the retrograde cooling path of the IVZ during the Late Mesozoic (for a compilation see Zingg et al. 1990; Hunziker et al. 1992). Because of the variably reduced length scales for argon diffusion in the deformed micas, the in-situ $^{40}Ar/^{39}Ar$ UV-laser ages provide information on the cooling history of the Pogallo mylonites during this time interval. Undeformed foliation-parallel type I porphyroclasts yield furnace step-heating ages of 182.7 ± 2.4 and 181.1 ± 2.2 Ma, whereas kinked and strongly deformed muscovites from the same sample were able to record a range of ages and thus reveal a much longer cooling history, both by incremental step-heating and in-situ UV-laser ablation dating. These results are consistent with the predictions of diffusion theory when applied to the concept of variably sized microstructurally controlled diffusion segments. Using the same model parameters as above (Kirschner et al. 1996), a change in diffusion length scale of one order of magnitude results in a ΔT_c of $\sim$100 °C. If we compare this to the spread of intra-granular $^{40}Ar/^{39}Ar$ apparent ages of about 50–60 Ma for type I muscovite, a cooling rate of 1–2 °C/Ma can be inferred for the Mid- to Late Jurassic. The difference in error-weighted average between biotite and muscovite apparent ages (147.7 ± 5.1 vs 123.3 ± 7.2 Ma; the error-weighted average is used only for comparison of the two in-situ $^{40}Ar/^{39}Ar$ data sets and obviously has no geological meaning) points consistently to the same cooling rate if one assumes a ΔT_c of about 50–70 °C for a muscovite–biotite pair. Mylonitic deformation thus produced a suite of sub-grain-sizes that, when sufficiently characterized by optical or electron microscopy, can provide additional information about the T–t history of a given sample.

On the basis of independent geological constraints, the ages obtained by furnace step-heating of undeformed porphyroclasts, and confirmed by the oldest in-situ $^{40}Ar/^{39}Ar$ data, are interpreted as the age of greenschist facies mylonitization along the Pogallo Shear Zone. This interpretation takes into account field observations documenting that post-greenschist facies Pogallo deformation along the contact of the IVZ and SCZ involved localized cataclasis (Handy 1987), which is consistent with syntectonic temperatures well below the closure temperature of 380–400 °C as calculated for undeformed type I porphyroclasts.

Conclusions

1. The inter- and intra-grain variation in apparent muscovite $^{40}Ar/^{39}Ar$ ages detected by in-situ UV-laser dating in strongly deformed muscovite of the PSZ reflects successive cooling through closure temperatures on the scale of microstructurally controlled diffusion segments. The observed intra-grain variability is attributed to variably sized and spaced segments within the muscovite that were formed by crystal plastic deformation processes. Mylonitization drastically reduced the effective length scale for argon diffusion by introducing major segment-bounding discontinuities in the mica lattice. The data presented here are consistent with volume diffusion-dominated argon loss on the scale of the microstructurally controlled diffusion segments and associated fast pathway diffusion along zones of high defect density and intra-granular microfractures.
2. Not only does deformation lower the argon closure temperature of micas by mechanically reducing the grain size and hence the diffusion radii on the grain scale (Goodwin and Renne 1991), it can also strongly affect argon isotope systematics on the sub-grain scale. Whereas an appropriate, intermediate diffusion length scale can be readily estimated from the observed grain size of mylonitic rocks, the complexity of a heterogeneous distribution of microstructurally controlled segment sizes documented for muscovite from the Pogallo mylonites can currently only be resolved with the high-spatial resolution of the UV-laser ablation microprobe.
3. Because deformation along the extensional PSZ occurred under decreasing temperature conditions, undeformed foliation forming muscovite porphyro-

clasts are expected to record the timing of greenschist facies mylonitization in the 380–400 °C temperature range. Therefore, the 182.0 ± 1.6 Ma error-weighted average of the plateau ages is interpreted as the age of greenschist facies deformation and associated uplift of the Ivrea-Verbano Zone.

4. The wide range of cooling ages recorded in the deformed muscovite and biotite from the shear zone mylonite allow us to estimate slow cooling rates of about 2 °C/Ma for the IVZ during the Late Jurassic and Early Cretaceous. Using nature as a laboratory for a long-term argon diffusion experiment, the in-situ UV-laser ablation $^{40}Ar/^{39}Ar$ data provide further constraints on the uplift and cooling history of intermediate crustal rocks of the IVZ where no other geo-/thermochronometer is currently applicable.

Acknowledgements This study was supported by the Swiss National Science Foundation (SNF grant 2000-056849 to M.A.C.) and the Deutsche Forschungsgemeinschaft (DFG grant Ha/2403-1 to M.R.H.). Comments by W.E. Hames, W.J. Dunlap, N. Kramar, and B. Hacker helped to clarify various aspects of this study. We would like to thank S. Sherlock and an anonymous reviewer for constructive reviews that improved the clarity of arguments presented in this paper.

References

Banos JO, Amouric M, DeFouquet C, Baronnet A (1983) Interlayering and interlayer slip in biotite as seen by HRTEM. Am Mineral 68:754–758

Bell IA, Wilson CJL, McLaren AC, Etheridge MA (1986) Kinks in mica: role of dislocations and (001) cleavage. Tectonophysics 78:201–228

Bertotti G, Picotti V, Bernoulli D, Castellarin A (1993) From rifting to drifting: tectonic evolution of the South-Alpine upper crust from the Triassic to the Early Cretaceous. Sediment Geol 86:53–76

Bertotti G, Seward D, Wijbrans J, ter Voorde M, Hurford AJ (1999) Crustal thermal regime prior to, during, and after rifting: a geochronological and modeling study of the Mesozoic South Alpine rifted margin. Tectonics 18:185–200

Bill M, Bussy F, Cosca MA, Masson H, Hunziker JC (1997) High-precision U–Pb and $^{40}Ar/^{39}Ar$ dating of an Alpine ophiolite (Gets nappe, French Alps). Eclogae Geol Helv 90: 43–54

Blavette D, Cadel E, Fraczkiewicz A, Menand A (1999) Three-dimensional atomic-scale imaging of impurity segregation to line defects. Science 286:2317–2319

Boriani A, Sacchi R (1973) Geology of the junction between the Ivrea-Verbano and Strona-Ceneri Zones (southern Alps). Mem Geol Mineral Univ Padova 28:1–35

Chacko T, Hu X, Mayeda TM, Clayton RN, Goldsmith JR (1996) Oxygen isotope fractionations in muscovite, phlogopite, and rutile. Geochim Cosmochim Acta 60(14):2595–2608

Dahl P (1996) The crystal chemical basis for Ar retention in micas: inferences from interlayer partitioning and implications for geochronology. Contrib Mineral Petrol 123:22–39

Dalrymple GB, Alexander EC, Lanphere MA, Kraker GP (1981) Irradiation of samples for $^{40}Ar/^{39}Ar$ dating using the Geological Survey TRIGA reactor. US Geol Surv Prof Pap 1176

Dodson MH (1973) Closure temperature in cooling geochronological systems. Contrib Mineral Petrol 40:259–274

Dunlap WJ (1997) Neocrystallization or cooling? $^{40}Ar/^{39}Ar$ ages of white micas from low-grade mylonites. Chem Geol 143 (3–4):181–203

Dunlap WJ, Kronenberg AK (2001) Argon loss during deformation of micas: constraints from laboratory deformation experiments. Contrib Mineral Petrol 141(2):174–185

Dunlap WJ, Teyssier C, McDougall I, Baldwin S (1991) Ages of deformation from K/Ar and $^{40}Ar/^{39}Ar$ dating of white micas. Geology 19:1213–1216

Giorgis D, Cosca MA, Li S (2000) Distribution and significance of extraneous argon in UHP eclogite (Sulu terrain, China): insights from in situ $^{40}Ar/^{39}Ar$ UV-laser ablation analysis. Earth Planet Sci Lett 181:605–615

Goodwin LB, Renne PR (1991) Effects of progressive mylonitization on Ar retention in biotites from the Santa Rosa mylonite zone (California), and thermochronologic implications. Contrib Mineral Petrol 108:283–297

Goodwin LB, Wenk HR (1990) Intracrystalline folding and cataclasis in biotite of the Santa Rosa mylonite zone: HVEM and TEM observations. Tectonophysics 172:201–214

Hames WE, Andresen A (1996) Timing of Paleozoic orogeny and extension in the continental shelf of north-central Norway as indicated by laser $^{40}Ar/^{39}Ar$ muscovite dating. Geology 24:1005–1008

Hames WE, Bowring SA (1994) An empirical evaluation of the argon diffusion geometry in muscovite. Earth Planet Sci Lett 124:161–167

Hames WE, Cheney JT (1997) On the loss of $^{40}Ar^*$ from muscovite during polymetamorphism. Geochim Cosmochim Acta 61:3863–3872

Handy MR (1987) The structure, age, and kinematics of the Pogallo fault zone, Southern Alps, northwestern Italy. Eclogae Geol Helv 80(3):593–632

Handy MR, Zingg A (1991) The tectonic and rheological evolution of an attenuated cross section of the continental crust: Ivrea crustal section, southern Alps, northwestern Italy and Switzerland. Geol Soc Am Bull 103:236–253

Handy MR, Franz L, Heller F, Janott B, Zurbriggen R (1999) Multistage accretion and exhumation of the continental crust (Ivrea crustal section, Italy and Switzerland). Tectonics 18(6): 1154–1177

Harrison TM, Heizler MT, Lovera OM, Chen W, Grove M (1994) A chlorine disinfectant for excess argon released from K-feldspar during step-heating. Earth Planet Sci Lett 123:95–104

Hodges KV, Bowring SA (1995) $^{40}Ar/^{39}Ar$ thermochronology of isotopically zoned micas: insights from the southwestern USA Proterozoic orogen. Geochim Cosmochim Acta 59(15): 3205–3220

Hodges KV, Fountain DM (1984) Pogallo Line, South Alps, northern Italy: an intermediate crustal level, low-angle normal fault? Geology 12:151–155

Hunziker JC, Desmons J, Hurford AJ (1992) Thirty-two years of geochronological work in the Central and Western Alps: a review on seven maps. Mém Géol Lausanne 13:1–59

Jaboyedoff M, Cosca MA (1999) Dating incipient metamorphism using $^{40}Ar/^{39}Ar$ geochronology and XRD modeling; a case study from the Swiss Alps. Contrib Mineral Petrol 35(2–3): 93–113

Janák M, Plasienka D, Frey M, Cosca MA, Schmidt ST, Luptak B, Meres S (2001) Cretaceous evolution of a metamorphic core complex, the Veporic unit, Western Carpathians (Slovakia): P–T conditions and in situ $^{40}Ar/^{39}Ar$ UV laser probe dating of metapelites. J Metamorph Geol 2:197–216

Kelley SP, Turner G (1991) Laser probe $^{40}Ar/^{39}Ar$ measurements of loss profiles within individual hornblende grains from the Giants range Granite, northern Minnesota, USA. Earth Planet Sci Lett 107:87–105

Kelley SP, Arnaud NO, Turner SP (1994) High-spatial resolution $^{40}Ar/^{39}Ar$ investigations using an ultra-violet laser probe extraction technique. Geochim Cosmochim Acta 58(16):3519–3525

Kirschner DL, Cosca MA, Masson H, Hunziker JC (1996) Staircase $^{40}Ar/^{39}Ar$ spectra of fine-grained white mica: timing and duration of deformation and empirical constraints on argon diffusion. Geology 24(8):747–750

Kontak DJ, Farrar E, McBride S, Martin RF (1996) Mineral chemistry and $^{40}Ar/^{39}Ar$ dating of muscovite from the East Kemptville Leucogranite, southern Nova Scotia; evidence for localized resetting of $^{40}Ar/^{39}Ar$ systematics in a shear zone. Can Mineral 33(6):1237–1253

Kramar N, Cosca MA, Hunziker JC (2001) Heterogeneous 40Ar* distributions in naturally deformed muscovite: in-situ UV-laser ablation evidence for microstructurally controlled diffusion. Earth Planet Sci Lett 192(3):377–388

Lee JKW (1993) The argon release mechanisms of hornblende in vacuo. Chem Geol 106:133–170

Lee JKW (1995) Multipath diffusion in geochronology. Contrib Mineral Petrol 120:60–82

Lister GS, Snoke AW (1984) S–C mylonites. J Struct Geol 6(6):617–638

Lee JKW, Onstott TC, Hanes JA (1990) An $^{40}Ar/^{39}Ar$ investigation of the contact effects of a dyke intrusion: Kapuskasing Structural Zone, Ontario: a comparison of laser microprobe and furnace extraction techniques. Contrib Mineral Petrol 105:87–105

Mares VM, Kronenberg AK (1993) Experimental deformation of muscovite. J Struct Geol 15:1061–1075

Masuda T, Morokawa T, Nakayama Y, Suzuki S (1997) Grain-boundary migration of quartz during annealing experiments at high temperatures and pressures with implications for metamorphic geology. J Metamorph Geol 15:311–322

Mulch A, Rosenau MR, Dörr W, Handy MR (2002) The age and structure of mafic and granitoid veins along the CMB-Line, Ivrea-Verbano and Strona-Ceneri Zones (southern Alps). Swiss Bull Mineral Petrol, (in press)

Passchier CW, Trouw RAJ (1996) Microtectonics. Springer, Berlin Heidelberg New York

Phillips D, Onstott TC (1988) Argon isotope zoning in mantle phlogopite. Geology 16:542–546

Reddy SM, Potts GJ (1999) Constraining absolute deformation ages: the relationship between deformation mechanisms and isotope systematics. J Struct Geol 21:1255–1265

Reddy SM, Kelley SP, Wheeler J (1996) A $^{40}Ar/^{39}Ar$ laser probe study of micas from the Sesia Zone, Italian Alps: implications for metamorphic and deformation histories. J Metamorph Geol 14:493–508

Reddy SM, Kelley SP, Magennis L (1997) A microstructural and argon laserprobe study of shear zone development at the western margin of the Nanga Parbat-Haramosh Massif, western Himalaya. Contrib Mineral Petrol 128:16–29

Reddy SM, Potts GJ, Kelley SP, Arnaud NO (1999) The effects of deformation-induced microstructures on intragrain $^{40}Ar/^{39}Ar$ ages in potassium feldspar. Geology 27(4):363–366

Reddy SM, Potts GJ, Kelley SP (2001) $^{40}Ar/^{39}Ar$ ages in deformed potassium feldspar: evidence of microstructural control on Ar isotope systematics. Contrib Mineral Petrol 141(2):186–200

Renne PR, Swisher CC, Deino AL, Karner DB, Owens TL, DePaolo DJ (1998) Intercalibration of standards, absolute ages and uncertainties in $^{40}Ar/^{39}Ar$ dating. Chem Geol 145:117–152

Rieder et al. (IMA Mica Subcommittee) (1999) Nomenclature of the micas. Mineral Mag 63(2):267–279

Rubatto D, Gebauer D, Fanning M (1998) Jurassic formation and Eocene subduction of the Zermatt-Saas-Fee ophiolites: implications for the geodynamic evolution of the Central and Western Alps. Contrib Mineral Petrol 132:269–287

Scaillet S, Féraud G, Lagabrielle Y, Ballèvre M, Ruffet G (1990) $^{40}Ar/^{39}Ar$ laser-probe dating by step-heating and spot fusion of phengites from the Dora Maira nappe of the western Alps. Geology 18:741–744

Schmid SM, Zingg A Handy MR (1987) The kinematics of movements along the Insubric Line and the emplacement of the Ivrea Zone. Tectonophysics 135:47–66

Sharp ZD (1992) In-situ laser microprobe techniques for stable isotope analysis. Chem Geol 101:3–19

Shea WT, Kronenberg AK (1992) Rheology and deformation mechanisms of an isotropic mica schist. J Geophys Res 97:15201–15237

Sherlock SC, Kelley SP, Inger S, Harris NBW, Okay AI (1999) $^{40}Ar/^{39}Ar$ and Rb–Sr geochronology of high-pressure metamorphism and exhumation history of the Tavsanli Zone, NW Turkey. Contrib Mineral Petrol 137:46–58

Sibson RH (1977) Fault rocks and fault mechanisms. J Geol Soc Lond 133:191–213

Simpson C, Schmid SM (1983) An evaluation of criteria to deduce the sense of movement in sheared rocks. Geol Soc Am Bull 94(11):1281–1288

Steiger RH, Jäger E (1977) Subcommission on geochronology: convention on the use of decay constants in geo- and cosmochronology. Earth Planet Sci Lett 36:359–362

Tullis J (1983) Deformation of feldspars. In: Ribbe PH (ed) Feldspar mineralogy. Reviews in mineralogy. Mineralogical Society of America, Washington, DC, pp 207–323

Vauchez A (1987) The development of discrete shear-zones in a granite: stress, strain and changes in deformation mechanisms. Tectonophysics 133:137–157

Villa IM (1994) Multipath Ar transport in K-feldspar deduced from isothermal heating experiments. Earth Planet Sci Lett 122:393–401

Villa IM, Grobéty B, Kelley SP, Trigila R, Wieler R (1996) Assessing Ar transport in the McClure Mountains hornblende. Contrib Mineral Petrol 126:67–80

West DP, Lux DR (1993) Dating mylonitic deformation by the $^{40}Ar/^{39}Ar$ method: an example from the Norumbega Fault Zone, Maine. Earth Planet Sci Lett 120:221–237

Wilson CJL, Bell IA (1979) Deformation of biotite and muscovite. Tectonophysics 58(1–2):179–200

Winterer EL, Bosellini A (1981) Subsidence and sedimentation on Jurassic passive continental margin, southern Alps, Italy. Am Assoc Petrol Geol Bull 65:394–421

Zingg A, Handy MR, Hunziker JC, Schmid SM (1990) Tectonometamorphic history of the Ivrea Zone and its relation to the crustal evolution of the Southern Alps. Tectonophysics 182:169–192